JOURNAL OF AIRCRAFT
Vol. 38, No. 6, November–December 2001

Computation of Viscous Flow for a Boeing 777 Aircraft in Landing Configuration

Stuart E. Rogers* and Karlin Roth†
NASA Ames Research Center, Moffett Field, California 94035
Hoa V. Cao‡
The Boeing Company, Seattle, Washington 98124
Jeffrey P. Slotnick§ and Mark Whitlock¶
The Boeing Company, Long Beach, California 90807
and
Steven M. Nash** and M. David Baker**
MCAT, Inc.; NASA Ames Research Center, Moffett Field, California 94035

A series of Navier–Stokes simulations of a complete Boeing 777-200 aircraft configured for landing is obtained using a structured overset grid process and the OVERFLOW computational fluid dynamics code. At approach conditions, the computed forces for the 777 computation are within 1.5% of experimental data for lift and within 4% for drag. The computed lift is lower than the experiment at maximum-lift conditions, but shows closer agreement at poststall conditions. The effect of sealing a spanwise gap between leading-edge elements and adding a chine onto the nacelle is computed at a high angle of attack. These additions make a significant difference in the flow over the wing near these elements. Detailed comparisons between computed and experimental surface pressures are shown. Good agreement is demonstrated at lower angles of attack, including a prediction of separated flow on the outboard flap.

Introduction

CALCULATING the viscous fluid flow over a high-lift system of a subsonic commercial aircraft is one of the most difficult problems in computational fluid dynamics (CFD). Even in two dimensions, state-of-the-art CFD codes fail to predict consistently, with sufficient accuracy, trends with Reynolds number or trends with flap/slat rigging changes.[1] High-lift flowfield analysis is also a very important problem for commercial aircraft companies; the payoffs for understanding it and designing a more efficient high-lift system for commercial jet transports are quite high.[2] Increases in lift coefficient *CL* and in lift-over-drag can lead to a simpler high-lift system, resulting in less weight and less noise, as well as increases in both payload and range.

The difficulties in simulating high-lift flows come from the severe complexity of both the geometry and the flowfield. The complexity of the flowfield stems from the wing having multielements with very small gaps between them, leading to an interaction of various viscous flow phenomena. As stated by Meredith,[2] these flow phenomena include boundary-layer transition, shock and boundary-layer interactions, viscous–wake interactions, confluent wakes and boundary layers, and separated flows. Because the fluid dynamics is dominated by viscous effects, only a high-fidelity simulation using the Navier–Stokes equations can provide the accuracy necessary to assist in aircraft design.

Under the integrated wing design (IWD) element of the NASA Advanced Subsonic Technology (AST) program, a significant effort was focused on developing the CFD software tools required to perform production level CFD analysis of three-dimensional high-lift systems on complete transport configurations. One of the program milestones was to perform a CFD analysis of an entire high-lift aircraft from CAD to postprocessed solution in 50 working days. This milestone was met with a simulation of a Boeing 777-200 landing configuration using an overset structured grid approach and newly developed scripting software.[3] This accomplishment is a reduction by an order of magnitude in the CFD process time over what was possible 3 years earlier.

In addition to cycle time issues, a number of other challenges faced by the AST high-lift CFD team were put forth in a report.[4] These issues account for the fact that the current predictive accuracy of three-dimensional Navier–Stokes methods for high-lift flows could not be readily assessed: There was a lack of sufficient three-dimensional experimental high-lift data; only a limited number of three-dimensional high-lift simulations had been conducted, and the available simulations had been done on relatively simple geometries; such simulations required significant computational and labor resources; and most viscous computational approaches were not able to simulate the complex geometries found on a high-lift aircraft configuration.

The success of the development of new overset CFD tools,[3] together with the computational and labor resources of the AST program, has removed many of these obstacles. The result is the ability to perform viscous CFD simulations for a number of complex high-lift configurations and compare them to experimental data, thus providing an accuracy assessment for Navier–Stokes applications to high-lift aircraft. In two companion papers, results are presented for the application of the overset CFD method to the flow over a high-wing transport aircraft with externally blown flaps[5] and the flow over a three-element trapezoidal wing.[6] The current work presents new results for the computed flow over a over a Boeing 777-200 aircraft configured for landing. The current work attempts to validate

Received 16 July 2000; presented as Paper 2000-4221 at the AIAA 18th Applied Aerodynamics Conference, Denver, CO, 14–17 August 2000; revision received 19 July 2001; accepted for publication 12 August 2001.

*Aerospace Engineer, NASA Advanced Supercomputing Division.
†Chief, Aerospace Operations Modeling Office. Senior Member AIAA.
‡Principal Engineer, Commercial Airplane Group.
§Principal Engineer, Subsonic Aerodynamics Technology. Senior Member AIAA.
¶Engineer/Scientist Specialist, Subsonic Aerodynamics Technology. Member AIAA.
**Research Engineer, Commercial.

the overset CFD approach for high-lift aircraft by comparing the computed results to experimental data obtained in the NASA Ames Research Center 12-Foot Pressure Wind Tunnel.

In the following sections, this paper presents the geometry and grids used in the current analysis, presents some initial results for the lift coefficient, shows the effects of sealing a spanwise gap between two leading-edge components and the effect of adding of a nacelle chine, and presents detailed pressure coefficient comparisons between computed and experimental data for several angles of attack.

Geometry and Grids

The computations simulate a 4.2%-scale, full-span model of the Boeing 777-200 aircraft as tested in the NASA Ames Research Center 12-Foot Pressure Wind Tunnel. A photograph of this model is shown in Fig. 1. The major aircraft components included in the computational and experimental models are the fuselage, the main wing, the inboard and outboard leading-edge slats, the Krueger slat, the inboard and outboard flaps, the flaperon, the flow-through engine nacelle and core cowl, the engine strut, and the vertical tail. Although landing gear is shown in Fig. 1, the CFD results were compared with experimental runs with the landing gear off. The experimental model also included a chine on the inboard side of the nacelle. Initially, CAD data for this component could not be found and so was not included. The definition of the chine was obtained later and then added to the computational model, as described in a later section. Other details of the model include steps along the leading edge of the main wing: the side-of-body (SOB) step, a step near the strut, and an outboard (OB) step near the wing tip. The surface grids for the SOB step and the OB step are shown in Figs. 2a and 2b, respectively.

To simplify the individual component grid generation, the seals between the flaps and flaperon are omitted. In the experiment, the flaps and flaperon are partially sealed together. This is done using wax and/or tape after the components are installed for each rigging. Thus, the CAD definition of the components do not represent the actual wind-tunnel model in this regard. As shown in Fig. 3, two small spanwise gaps (about 0.5% of the mean aerodynamic chord) are present between the flap elements in the computational model. It was anticipated that these small gaps would only have a minor effect on the flow solution. The inboard end of the inboard flap is partially sealed against the fuselage in the wind-tunnel model. In contrast, it was expected that this seal would have a nonnegligible effect on the flow. Therefore, the sealing of the inboard flap against the fuselage was modeled in the computation.

At the leading edge, in the vicinity of the strut, Fig. 4 shows a closeup of the surface grids on the wing leading edge, the Krueger slat, and the inboard slat. Small gaps exist at either end of the Krueger for the CFD model, whereas for the wind-tunnel model, the spanwise ends of the Krueger were partially sealed against the strut and inboard slat with wax and tape. These small gaps allow the grid generation for each component to proceed independent of the placement of neighboring components. The ends of the flap and slat elements are resolved using wingcap grids that in previous work[7] have been shown to resolve adequately the geometry and near-body flowfield.

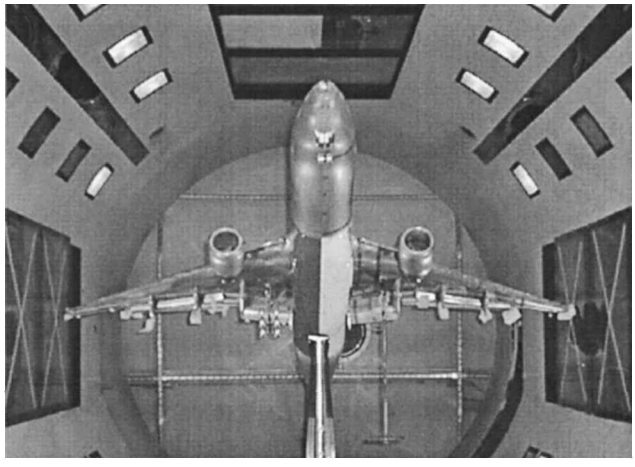

Fig. 1 Boeing 777-200 wind-tunnel model.

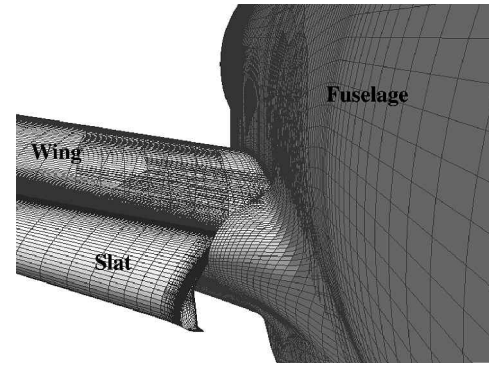

a) SOB step

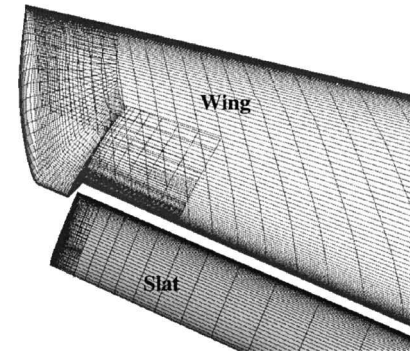

b) OB step

Fig. 2 Spanwise steps in the wing leading edge.

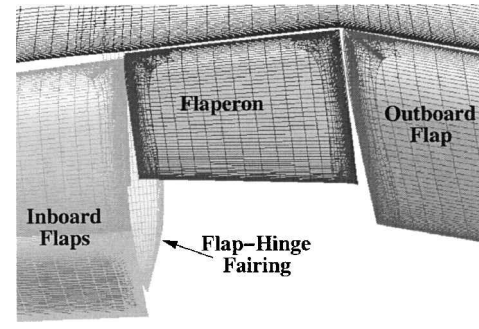

Fig. 3 Gaps between flaps and flaperon.

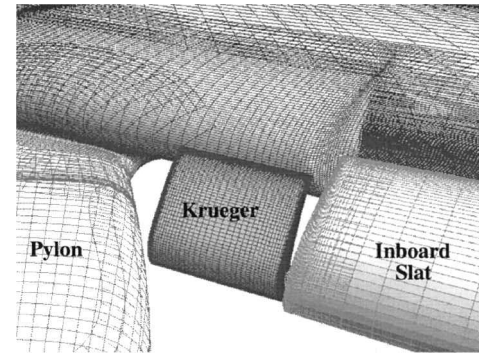

Fig. 4 Leading-edge spanwise gaps.

Both the leading-edge and trailing-edge brackets are omitted from the CFD model. Trailing-edge flap–bracket fairings are expected to have a larger impact on the flow than the brackets, and so the three largest flap–bracket fairings are included in the computational simulation: the outboard fairing on the inboard flap and the inboard and outboard fairings on the outboard flap. A closer view of the inboard fairing is shown in Fig. 5. The fairings are positioned with

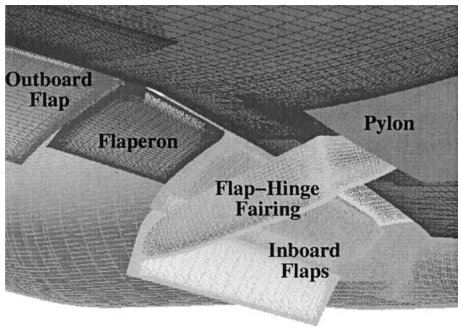

Fig. 5 Inboard flap-bracket fairing.

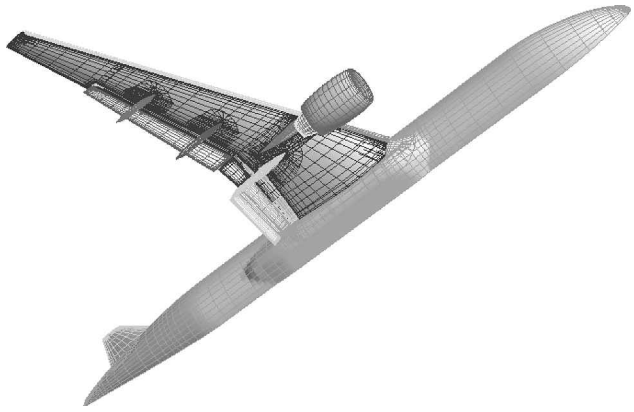

Fig. 6 Surface grids on Boeing 777-200.

and sealed against the underside of the wing, but are not connected to the flap surface.

The entire grid system for the Boeing 777-200 was generated on an SGI Octane workstation, with two R10000 195-MHz processors, 896 MB of memory, and 13 GB of disk space. The execution of the script system that runs the entire grid-generation process from the original surface definition to the final grid system requires 5 h on this machine. The resulting grid system for the Boeing 777-200 aircraft configured for landing consists of 22.4×10^6 grid points within 79 overset zones. A view of the surface grids on the entire configuration is shown in Fig. 6, which plots only every fourth grid line in each computational direction for clarity. An attempt was made to generate grids that would be adequate for all expected flow features based on previous high-lift CFD problems, most of which were simulations of two-dimensional multielement airfoils. Grid spacing of 10^{-6} times the mean aerodynamic chord is applied normal to the surface. This results in y^+ values on the order of 1.0 for the first grid point off the surface. Also, the maximum grid-stretching ratio in the normal direction is limited to 1.25. A total of 5617 orphan points (approximately 0.02% of the total points) remained within the grid system after the overset process; averaging is used to update these points within the flow solver. An orphan point is a boundary point requiring interpolated solution data from a neighboring grid, but for which the software cannot find a neighbor grid with adequate overlap.

B777 Flow Simulation and Analysis

Flow Solver

The OVERFLOW[8,9] Navier–Stokes flow solver was used in all of the current computations. This code is written to be efficient for computing very large-scale CFD problems on a wide range of supercomputer architectures. On vector supercomputers with very fast secondary memory devices, the OVERFLOW code includes an out-of-core memory management option, such that the total memory used is a function of the largest zone in the grid system, not the total number of grid points. The code is efficiently vectorized and is written to execute simultaneously on multiple shared-memory processors. For cache-based multiple-processor machines, the code has been parallelized using both a shared memory algorithm, and with a message-passing interface library for nonshared memory systems. For more details, see the works by Jespersen[10] and Taft.[11] Approximately half of the current cases were run using the standard OVERFLOW, version 1.8b, whereas the rest of the cases were run using OVERFLOW-multi-level parallelization (MLP) version 1.8k. The former cases were run on a 16 processor Cray C90 computer, and the MLP version was run on an SGI ORIGIN 2000 machine with 256 processors.

All of the current OVERFLOW computations utilized the third-order Roe upwind–differencing[12] option, and the Spalart–Allmaras turbulence model[13] with the flow assumed to be fully turbulent. In the experimental investigation of the 777, no boundary-layer trips were used, and there was no measurement of transition locations. The prediction and modeling of transition for complex three-dimensional geometries is beyond the capability of the OVERFLOW code. The viscous terms in all three directions are computed; however, the cross-derivative viscous terms were not included. These were not used because they add about 10% to the cost of the computation and because previous test cases have shown that their use does not affect the solution. The multigrid option[9] to the code was used with three levels. Each OVERFLOW case is run using a local time-step scale of 0.1, a minimum Courant–Friedrichs–Lewy (CFL) number cutoff for the locally varying time stepping of 5.0, and a CFL number multiplier for the turbulence model of 4.0. Low Mach number preconditioning is not used because this option caused the code to become unstable for the 777 grid system. In these computations, the code was considered converged to a steady state when the $L2$ norm of the right-hand side had dropped at least two or three orders of magnitude for each computational grid and when the variation in the total lift coefficient was less than 0.01% over the last 100 cycles.

Flow Conditions

The simulation conditions for the current analysis corresponded to data acquired during wind-tunnel run 421 in the NASA Ames 12-Foot Pressure Wind Tunnel. The model was configured for landing as defined by the flaps-30 setting. The flow had a freestream Mach number of 0.2, a total pressure of 4.5 atm, and a Reynolds number based on the mean aerodynamic chord of 5.8×10^6. The simulation was conducted in free air; no wind-tunnel mounting hardware was modeled. The experimental data used for the comparisons were corrected for wind-tunnel wall and blockage interference, but exclude tare and interference corrections for the bipod mounting device.

Five solutions were computed using the grid system for the initial geometry. These were computed at angles of attack α of 4, 8, 12, 16, and 20 deg. The cases at $\alpha = 4$ and 8 deg were restarted from solutions obtained on an initial grid system that did not include the flap–bracket fairings. Such restarts save only a small percentage of the computing time compared to the freestream initial conditions, even though the change from the restarted solution is small. As a point of reference, the difference in CL at $\alpha = 8$ deg with the addition of the flap fairings was 1.8% lower, and the drag coefficient CD was 1.5% lower. Figure 7 shows the convergence history for CL for the cases computed at 4-, 8-, and 12-deg angle of attack. Because of the proprietary nature of these data, the values cannot be included on the y axis of this and other subsequent plots of lift, drag, and pressure coefficients. However, these figures (7, 13, 14, 16–21) that

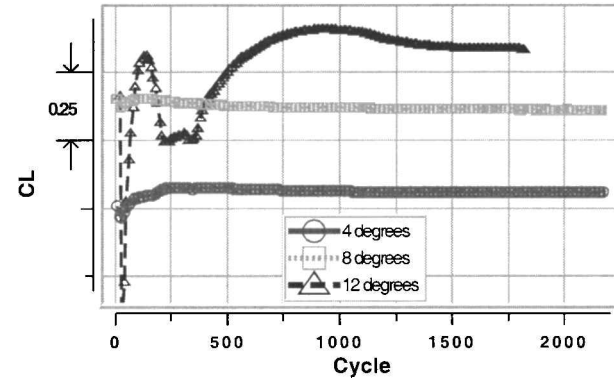

Fig. 7 Convergence of lift coefficient.

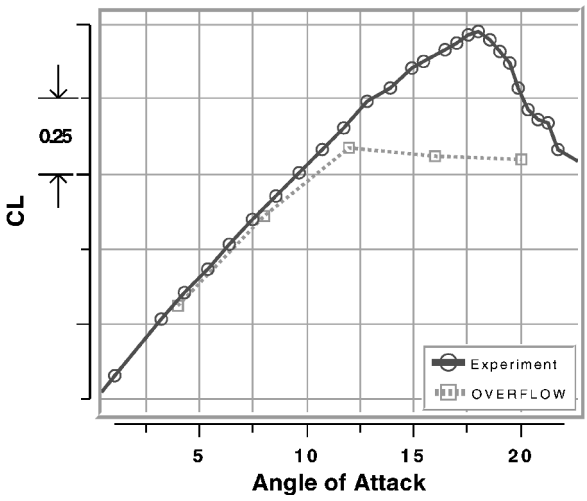

Fig. 8 Lift coefficient vs angle of attack.

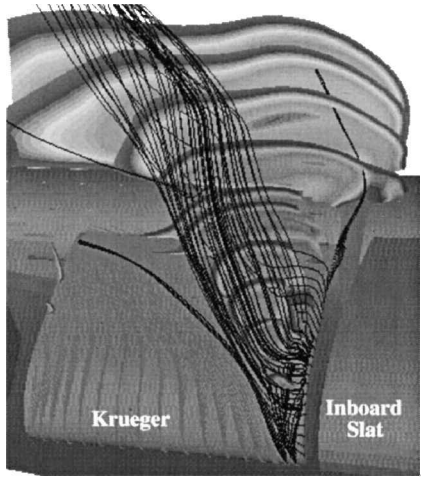

a) Close view of flow over Krueger

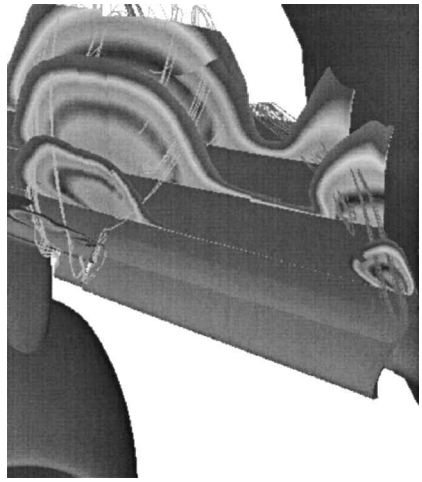

b) View of inboard portion of wing

Fig. 9 Mach contours and particle traces at $\alpha = 16$ for initial geometry.

plot these quantities do include a label of the increment between the major tick marks on the vertical axes. These three cases converged in an average of 2160 cycles and required an average of 194 C90 CPU hours per case. This convergence rate is fairly typical of all runs; however, the cases at higher angles of attack usually require more cycles.

The lift polars for the first five runs are plotted in Fig. 8. The computed *CL* differs from the experimental lift by less than 2% for the lower angles of attack. However, Fig. 8 shows that the computed

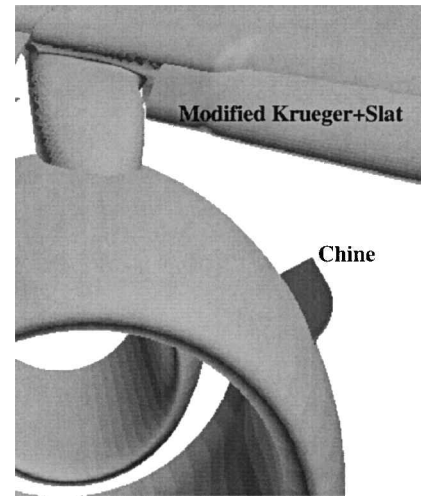

Fig. 10 Modified Krueger and inboard slat, and the chine mounted on the nacelle.

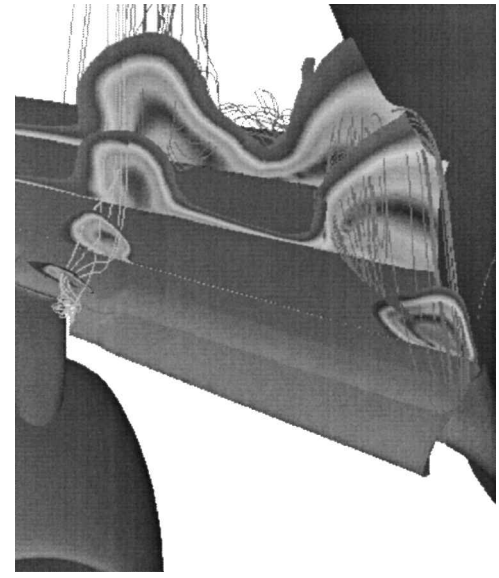

Fig. 11 Mach contours and particle traces at $\alpha = 16$ for sealed Krueger and slat.

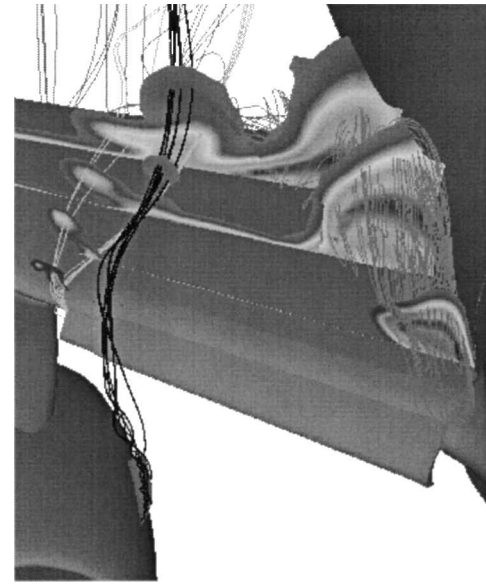

Fig. 12 Mach number and particle traces at $\alpha = 16$ with addition of chine.

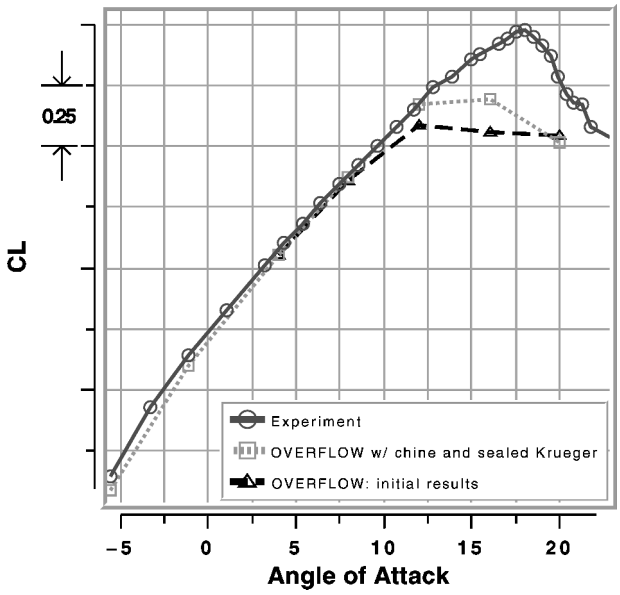

Fig. 13 Lift coefficient vs α.

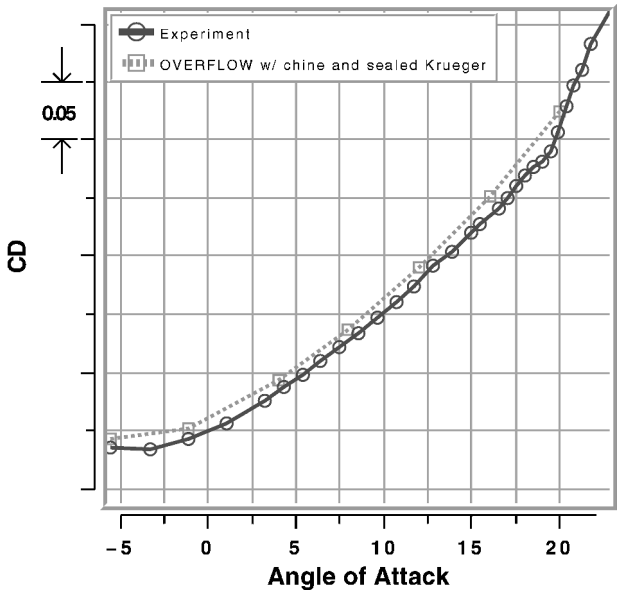

Fig. 14 Drag coefficient vs α.

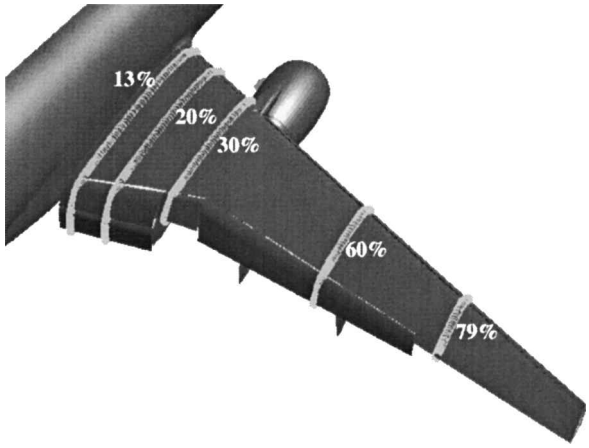

Fig. 15 Spanwise locations of the *Cp* data.

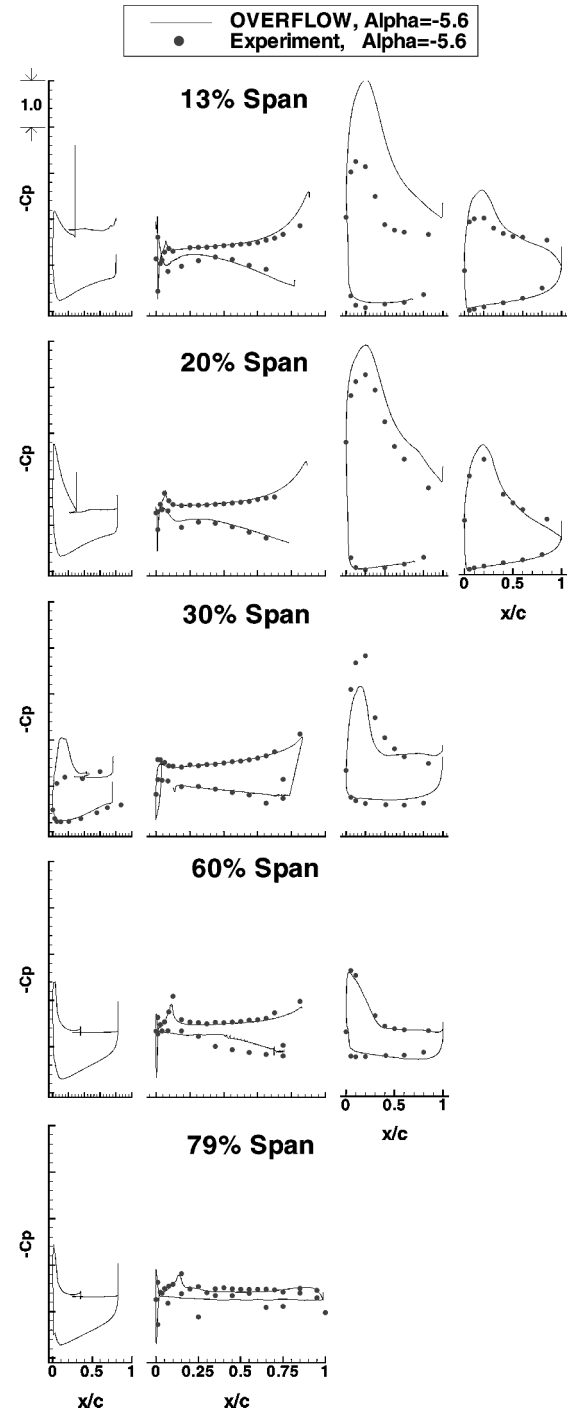

Fig. 16 *Cp* data for $\alpha = -5.6$ deg.

flow stalls at a much lower angle of attack than the experiment. Further investigation of the solution at $\alpha = 16$ deg shows that the Krueger slat experiences separated flow.

Figure 9 shows a closeup of the flow over the Krueger using both particle traces and Mach number contours. The solid Mach number contours are drawn in the range of 0.0–0.1, and show regions of slower flow. Figure 9 shows how a vortex is formed by flow traveling upward through the small gap between the Krueger and the inboard slat. This vortex flows over the top of the Krueger, lifting the flow off the surface of the Krueger, causing the flow to separate. In Fig. 9b, it can be seen that, as this passes onto the upper surface of the wing, the adverse pressure gradient causes rapid expansion, creating a large stall region on top of the wing.

These results suggest that one source of the discrepancy between the computations and the experiment at high angles of attack is

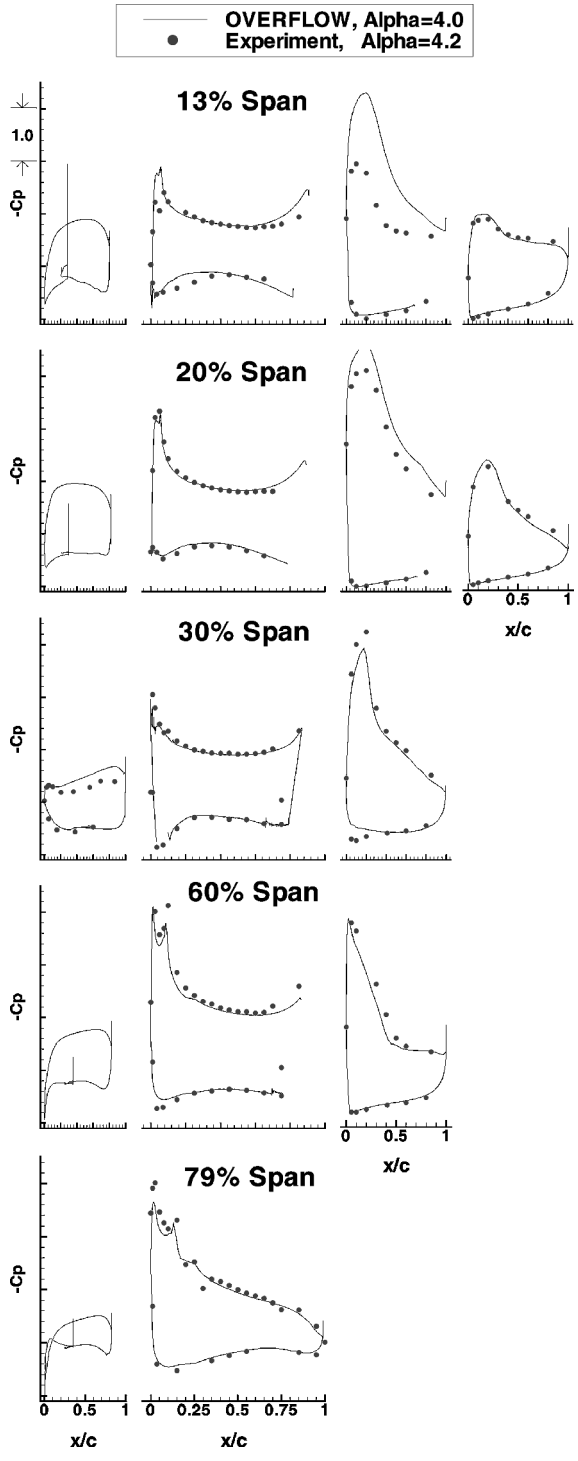

Fig. 17 *Cp* data for $\alpha = 4$ deg.

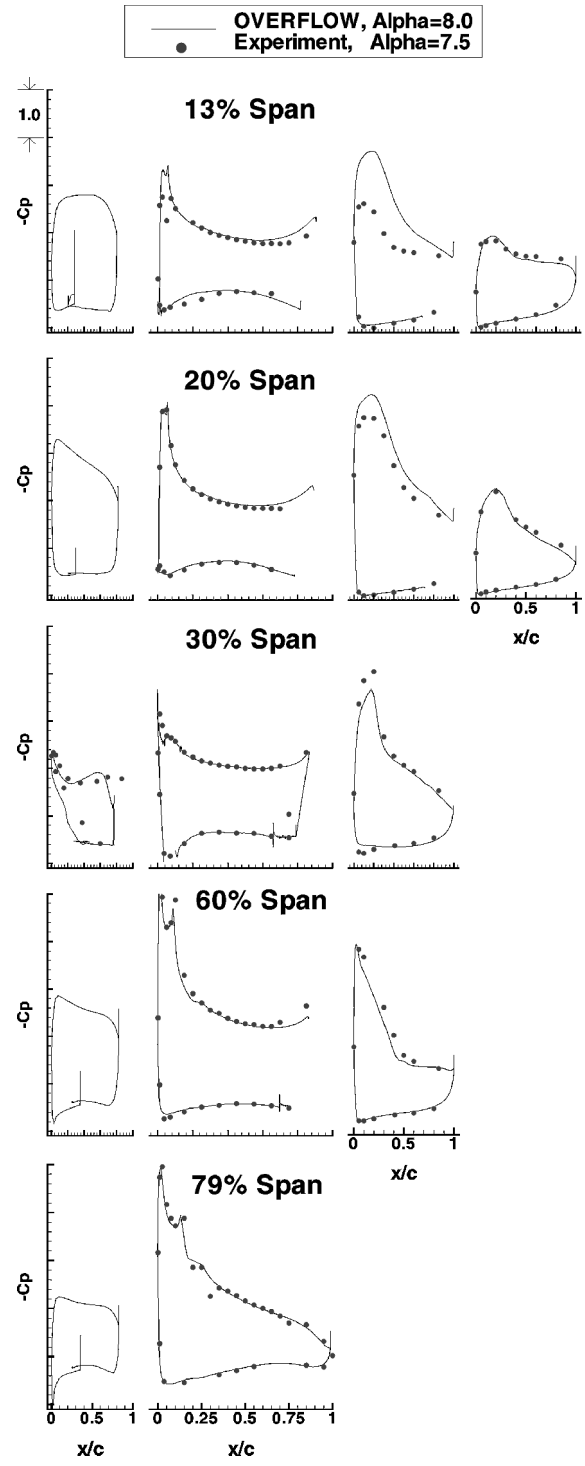

Fig. 18 *Cp* data for $\alpha = 8$ deg.

the small spanwise gap in the computational model between the Krueger slat and the inboard slat. In the experiment, this gap is partially sealed using tape and wax; the exact experimental geometry is difficult to duplicate. In an effort to seal this gap, the two elements were combined into a single inboard slat element, which creates the maximum amount of sealing possible. This modification required a slight rounding of the wing leading-edge step. Figure 10 shows an image of the modified Krueger and inboard slat.

A second grid system was built with this geometry modification, and a flow case was run at an angle of attack of 16 deg. The lift coefficient for this new run was only about 3% higher than the preceding case, and so the result was not as dramatic as expected. At the time this case was run, a CAD representation of the nacelle chine was finally located, and so this piece of the geometry was added to the computational model. Figure 10 shows the chine mounted on the inboard side of the nacelle. A third grid system was built with the chine added to the second grid system, and another case was run at an angle of attack of 16 deg. This resulted in a *CL* that was about 5% higher than the first grid system calculation at this angle of attack, which is still significantly lower than the experimental lift. A single grid was used to add the chine, which provided resolution for the near wake of the chine, but did not provide extra resolution for the vortex as it convects downstream over the wing. Although the wing grid has adequate off-body resolution for the slat wake, the chine vortex may not have adequate grid resolution.

Figures 11 and 12 show plots of Mach number contours and particle traces over the inboard region of the wing for these two geometry modifications. Figure 11 includes just the sealing of the

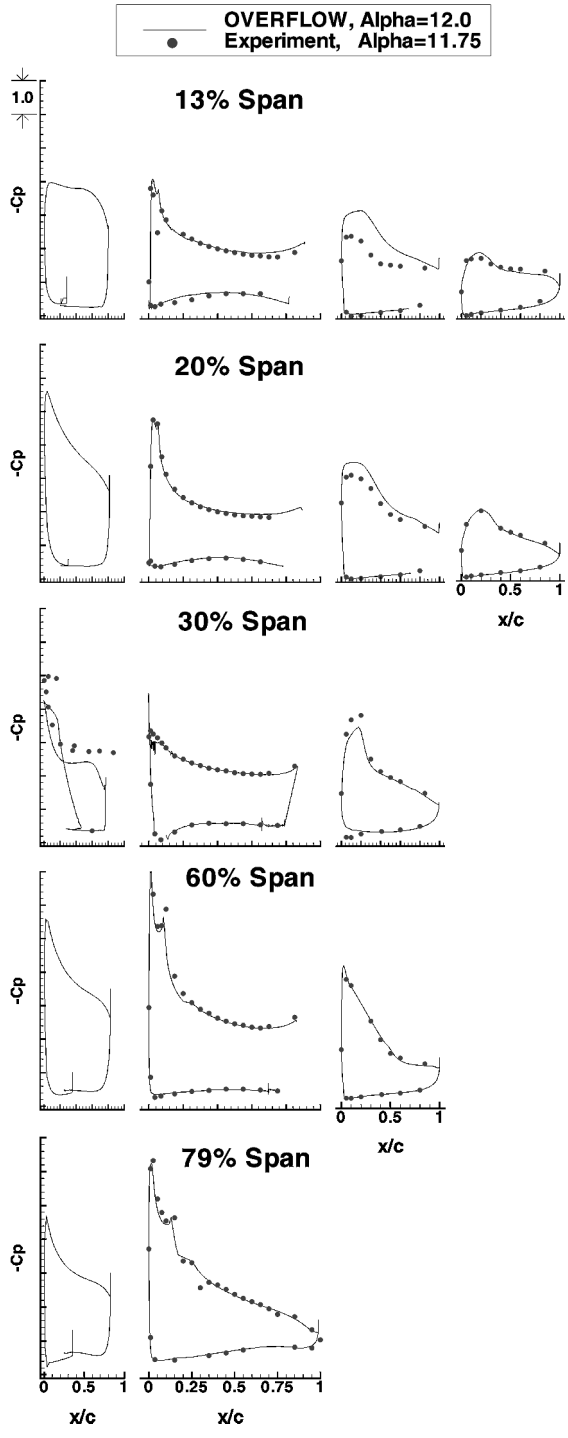

Fig. 19 *Cp* data for $\alpha = 12$ deg.

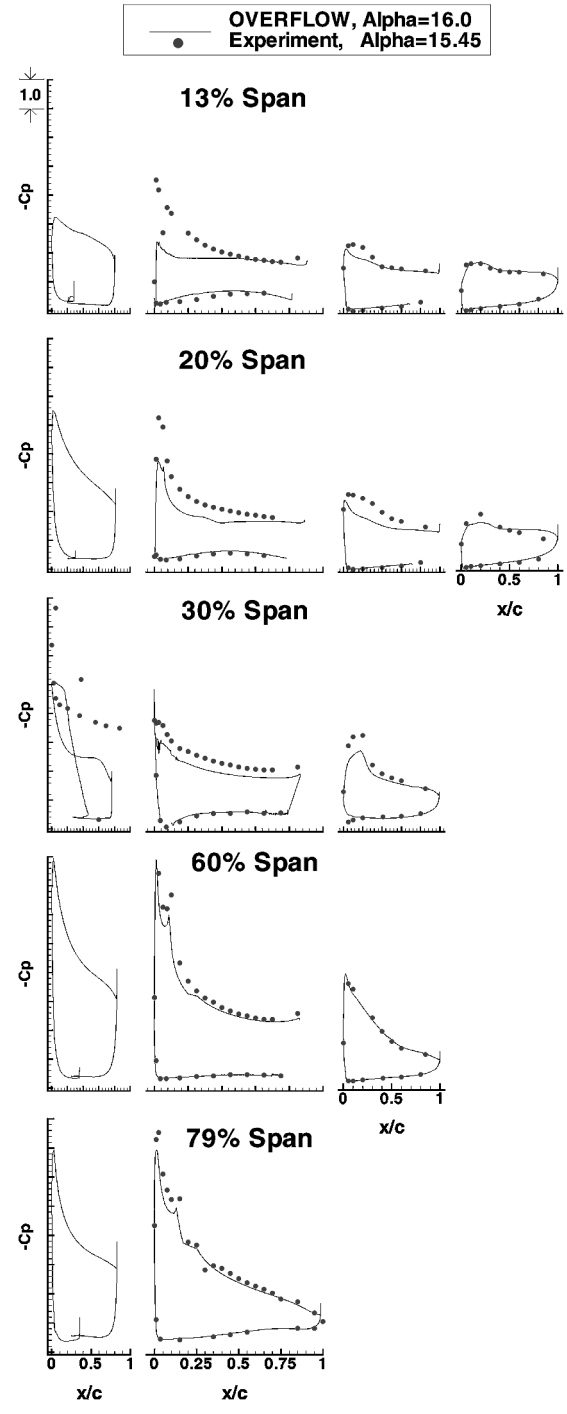

Fig. 20 *Cp* data for $\alpha = 16$ deg.

Krueger and slat spanwise gap, and Fig. 12 shows the flow after addition of the chine to this geometry. The sealing of the slats does reduce the amount of low-speed flow over the wing aft of the strut; however, it also increases the amount of separated flow at the wing root. The addition of the chine further reduces the amount of low-speed air aft of the strut and nacelle.

The third geometry with the sealed slats and the chine was also used to compute the flow at angles of attack of -5.5, -1.1, 4, 8, 12, and 20 deg. The lift coefficient vs angle of attack is plotted in Fig. 13 for this geometry, together with the experimental results and the results from the first geometry. Figure 14 shows *CD* vs α. The results from the third geometry show even better agreement with experimental lift for the lower angles of attack; at $\alpha = 4$, 8, and 12, the differences in lift are all less than 1.5%, and the differences in drag average 4%.

Pressure Coefficient Results

The pressure coefficient *Cp* data is presented for the third geometry. The *Cp* data are plotted for spanwise locations of 13, 20, 30, 60, and 79%; these locations are shown in Fig. 15.

In Figs. 16–21, *Cp* is plotted vs the scaled chordwise coordinate x/c, where c is the local chord for the particular element. The x axes are scaled differently for the slat, wing, and flaps so that data for the smaller elements can be seen. The first column in the plot is the slat, the second is the main wing, and the remaining columns are the flaps. The CFD results are plotted with solid lines, and the experimental results are plotted with circles. Within each of Figs. 16–21, the *Cp* scale is the same for all of the spanwise cuts. The computational results are compared with experimental data from the nearest corrected angle of attack available. The reason that many of the cases were computed at angles of attack not corresponding to a corrected

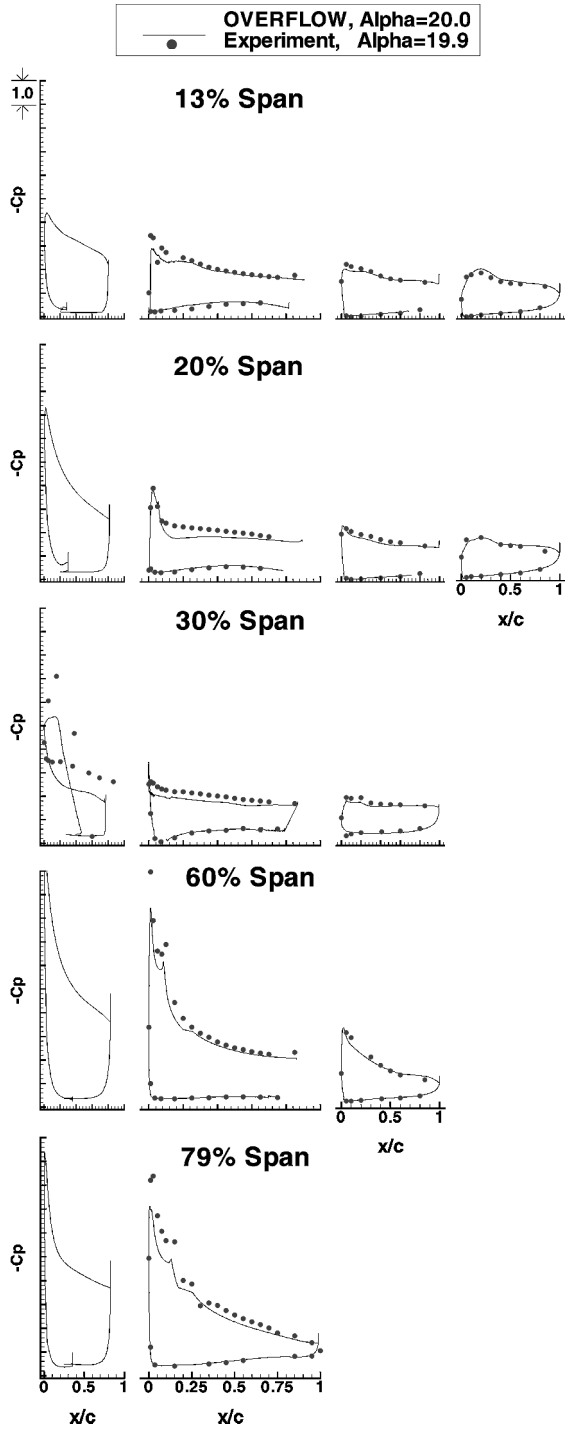

Fig. 21 *Cp* **data for α = 20 deg.**

experimental α is that none of the experimental data were made available to the high-lift CFD team until after several cases were initially computed. Note that the only experimental data available for the leading-edge devices are on the Krueger at the 30% span station.

The *Cp* data are plotted in Figs. 16–21 for angles of attack of −5.5-, 4-, 8-, 12-, 16-, and 20-deg angle of attack. In general, good agreement is seen between the experiment and the computations. One region in which there is consistently a difference is on the inboard end of the leading inboard flap, on the upper surface. Here, the computed suction peak is consistently higher than the experimental results, producing more lift in the computations on the leading inboard flap and the main wing than in the experiment. This location is very close to the rear bipod support in the experimental model, which includes a very large hole on the underside of the fuselage near this flap. This is a possible cause for this discrepancy. Other than this difference, the agreement between the experiment and computation for $\alpha = 4$, 8, and 12 is excellent. In particular, the indication of flow separation on the outboard flap is seen at 60% span in both the experiment and the computation by a flat section in the pressure curve over the aft portion of the upper surface at these angles of attack.

Figure 20 shows the results at 16-deg angle of attack. The inboard *Cp* data show a picture consistent with Fig. 12: The computed flow is stalled at the wing root. The experimental *Cp* data show a much higher leading-edge suction peak, indicating that it has not stalled at the wing root.

Figure 21 shows *Cp* data at 20-deg angle of attack. This shows that in both the experiment and the computed flow, the wing is stalled at all of the inboard sections, but still attached at the outboard sections. The computed upper surface pressures are consistently higher than the experiment, and thus, the computed lift is too low.

The reason for this large discrepancy at higher angles of attack is not known at this time. Possible reasons for the early stalling of the CFD model include a discrepancy between the computational and experimental geometries, inadequacies in the turbulence modeling, transition effects, insufficient grid resolution in the wing-root region or at the inboard end of the inboard slat, and wind-tunnel effects, including both wind-tunnel walls and bipod mounting effects. The possibility of a difference in the geometry is an issue, even though it is believed that the computational model of the inboard slat is trimmed at the same inboard plane as the experimental model, a small difference in the spanwise extent of this element can greatly effect the flow over the wing root. Given additional time and resources, the first thing to try would be to extend the inboard slat spanwise so that it seals against the fuselage, which should maximize the lift generated by the inboard wing.

Conclusions

An overset approach has been used to compute the flow over an entire Boeing 777-200 aircraft configured for landing. The computed results have been compared with experimental data acquired in the NASA Ames 12-Foot Pressure Wind Tunnel. Good agreement between the two is seen for the lift and drag coefficients at lower angles of attack: At approach conditions, the computational lift is within 1.5% of the experiment and the computed drag is within 4%. However, the computational model underpredicts the lift at higher angles of attack and misses maximum lift by nearly 11%. Several differences between the experimental model and the computational geometry exist. Most of these differences involve spanwise gaps between high-lift elements that are not present in the wind-tunnel model. The effect of completely sealing the gap between the inboard slat and the Krueger slat was demonstrated, as was the effect of adding the inboard chine. Both had a dramatic effect on the flow over the wing aft of the strut and nacelle, but did not dramatically increase the lift as the flow over the wing root began to stall.

The current work represents a big improvement in the ability to perform viscous CFD analysis of high-lift aircraft. The use of the overset-grid approach makes it possible to develop a grid system for a complete high-lift aircraft in several working weeks, which can then be used to study design tradesoffs with only a few days of work. The computational cost of computing numerous conditions, however, is substantial. The accuracy of the current approach is excellent at lower angles of attack, but the inability to compute maximum lift will limit the usefulness of viscous CFD analysis as a production design tool. Further work needs to be done to understand the reason for the poor agreement at maximum-lift conditions.

Acknowledgments

This work was partially funded by the Advanced Subsonic Technology Program (AST) through NASA Contract NAS2-20268. The authors would like to acknowledge the technical help of Pieter Buning, NASA Langley Research Center, as well as the AST/Integrated Wing Design program management for their dedication and insight.

They also wish to acknowledge the helpful comments from Thomas Coakley and Scott Lawrence in their review of this work.

References

[1]Lynch, F. T., Potter, R. C., and Spaid, F. W., "Requirements for Effective High Lift CFD," *Proceedings of the 20th Congress of the International Council of the Aeronautical Sciences*, Vol. 2, AIAA, Reston, VA, Sept. 1996, pp. 1479–1482.

[2]Meredith, P. T., "Viscous Phenomena Affecting High-Lift Systems and Suggestions for Future CFD Development," *High-Lift System Aerodynamics*, CP-515 AGARD, Paper 19, Sept. 1993.

[3]Rogers, S. E., Roth, K., Nash, S. M., Baker, M. D., Slotnick, J. P., Cao, H. V., and Whitlock, M., "Advances in Overset CFD Processes Applied to Subsonic High-Lift Aircraft," AIAA Paper 2000-4216, Aug. 2000.

[4]Bussoletti, J., Johnson, P., Jones, K., Roth, K., Slotnick, J. P., Ying, S., and Rogers, S. E., "The Role of Applied CFD within the AST/IWD Program High-Lift Subelement: Applications and Requirements," Advanced Subsonic Technology/Integrated Wing Design, AST/IWD Program Rept., June 1996.

[5]Slotnick, J. P., An, M. Y., Mysko, S. J., Yeh, D. T., Rogers, S. E., Roth, K., Baker, M. D., and Nash, S. M., "Navier–Stokes Analysis of a High-Wing Transport High-Lift Configuration with Externally Blown Flaps," AIAA Paper 2000-4219, Aug. 2000.

[6]Rogers, S. E., Roth, K., and Nash, S. M., "CFD Validation of High-Lift Flows with Significant Wind-Tunnel Effects," AIAA Paper 2000-4218, Aug. 2000.

[7]Rogers, S. E., Cao, H. V., and Su, T. Y., "Grid Generation for Complex High-Lift Configurations," AIAA Paper 98-3011, June 1998.

[8]Buning, P. G., Jespersen, D. C., Pulliam, T. H., Chan, W. M., Slotnick, J. P., Krist, S. E., and Renze, K. J., "OVERFLOW User's Manual, Version 1.8b," NASA Langley Research Center, Hampton, VA, 1998.

[9]Jespersen, D. C., Pulliam, T. H., and Buning, P. G., "Recent Enhancements to OVERFLOW," AIAA Paper 97-0644, Jan. 1997.

[10]Jespersen, D. C., "Parallelism and OVERFLOW," National Academy of Sciences, NAS TR NAS-98-013, URL: http://www.nas.nasa.gov/Pubs/TechReports/NASreports/NAS-98-013/ [cited Oct. 1998].

[11]Taft, J., "OVERFLOW Gets Excellent Results on SGI Origin2000," *NAS News*, Vol. 3, No. 1, URL: http://www.nas.nasa.gov/Pubs/NASnews/98/01/overflow.html [cited Jan. 1998].

[12]Roe, P. L., "Approximate Riemann Solvers, Parameter Vectors, and Difference Schemes," *Journal of Computational Physics*, Vol. 43, 1981, pp. 357–372.

[13]Spalart, P. R., and Allmaras, S. R., "A One-Equation Turbulence Model for Aerodynamic Flows," AIAA Paper 92-0439, Jan. 1992.